Electronic Supplementary Material (ESI) for Journal of Materials Chemistry A.
This journal is © The Royal Society of Chemistry 2021

Title: Unraveling two-phase transport in porous transport layer materials for polymer electrolyte water electrolysis

Salvatore De Angelis[1, #], Tobias Schuler[1, #], Margarita A. Charalambous[1], Federica Marone[2], Thomas J. Schmidt[1,3], Felix N. Büchi[1]

[1] Electrochemistry Laboratory, Paul Scherrer Institute, CH-5232 Villigen PSI, Switzerland.

[2] Swiss Light Source, Paul Scherrer Institute, CH-5232 Villigen PSI, Switzerland

[3] Laboratory of Physical Chemistry, ETH Zurich, CH-8093 Zurich, Switzerland.

[#] authors contributed equally to the manuscript.

E-mail of the corresponding author: felix.buechi@psi.ch

Supplementary materials

Ring artifact correction

Ring artifacts are arguably among the most pervasive artifacts present in reconstructed images from X-ray tomography. Generally, they appear as circular or semi-circular stripes in the reconstructed images. In X-ray tomographic microscopy (XTM), ring artifacts are due to imperfection in the optical and detector systems such as deformation of the magnifying lenses, non-uniform detector response, dead or miscalibrated pixels[1].

Several methods have been proposed for ring artifacts removal, including advanced flat-field corrections[2] or algorithms applied in both sinograms[3], and reconstructed domain[4]. However, ring artifacts can arise from several different causes and, sometimes, are specific to the employed X-ray hardware or sample. Therefore, most of the reported methods do not guarantee satisfactory results in images acquired for all possible experimental conditions.

In this work, we developed a ring artifact removal algorithm that works in the reconstruction domain, correcting directly the difference images.

The core of our method is the creation of a "ring-artifact mask" to be subtracted from the original image for achieving a ring-free image. Figure S1 shows the results (applied to an example slice) of the different steps for obtaining the ring artifact mask. The algorithm is divided into the following steps:

1. The original image (Figure S1 a) is transformed in polar coordinate (Figure S1 b), where the horizontal axis represents the angular intervals performed during the tomographic acquisition. The center of the polar transformation corresponds to the geometric center of the original image.
2. Each row of the polar image is processed by a 1D gaussian filter, in ϑ direction, resulting in Figure S1 c.

3. The result of step 2 is then filtered using a Savitzky-Golay (SV) polynomial filter, applied in the y-direction. The SV-filtered image is then subtracted to the gaussian-filtered image to achieve a clean ring-artifacts mask (Figure S1 d).
4. The result of step 3 is transformed back to Cartesian coordinates and substracted to the original image.

In summary, the polar transformation (step 1) allows transforming ring-shaped artifacts in horizontal stripes, easier to detect and correct. The 1D gauss filter (step 2) aims at blurring the original features while minimizing its effect on the horizontal stripes (polar transformed ring artifacts). For obtaining a clean ring artifact mask, with a flat background having near-zero values, the gauss-filtered image is processed using a Saviztky-Golay polynomial filter (in the y-direction) which extracts the low-frequency regions (associated with the background). Subtracting the result of the SV filter process to the gauss-filtered image, Figure S1 c is achieved (step 3). Finally, the obtained ring artifacts mask is subtracted from the original image to achieve the final ring corrected image. Figure S2 shows the results of the algorithm applied to the same slice presented in Figure S1.

The developed method requires two input parameters, the standard deviation of the gauss kernel *W1* and the frame size of the SV filter *F* (always odd). The polynomial order employed for the SV filter is 2. The input values have to be optimized for each different case (different samples, X-ray hardware, or experimental conditions). In this work, *W1*=201 and *F*=51 were found to give the best results.

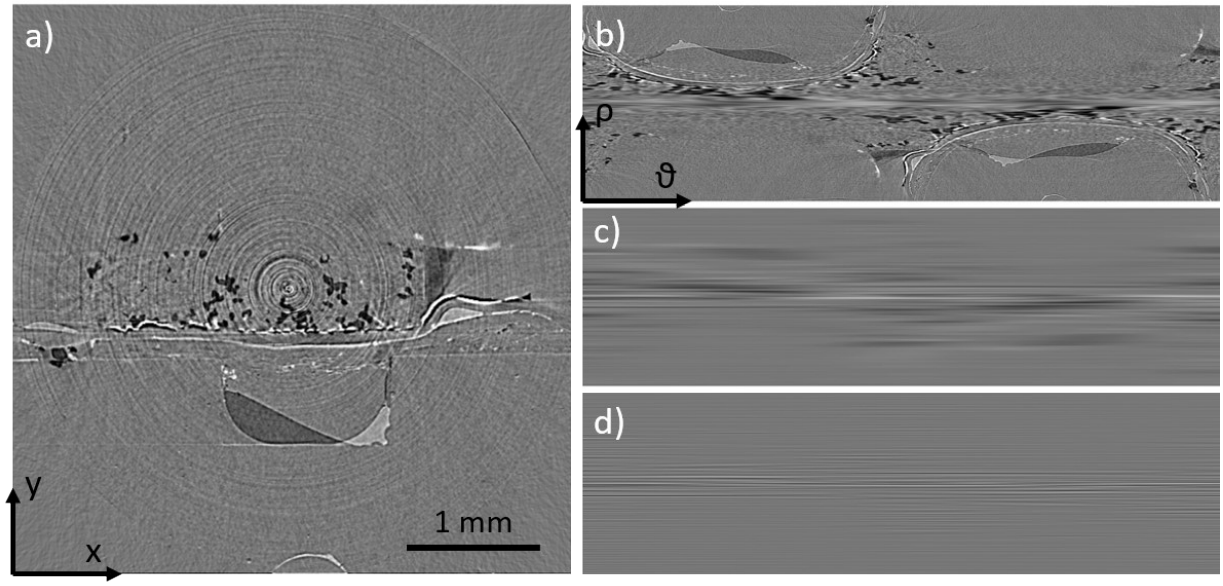

Figure S1. Intermediate results of the ring correction algorithm. a) Original image; b) original image in polar coordinate. The horizontal axis represents the angular steps employed in the tomographic procedure; c) gauss-filtered image obtained from step 2; d) ring artifacts mask (in polar coordinates) obtained from step 3.

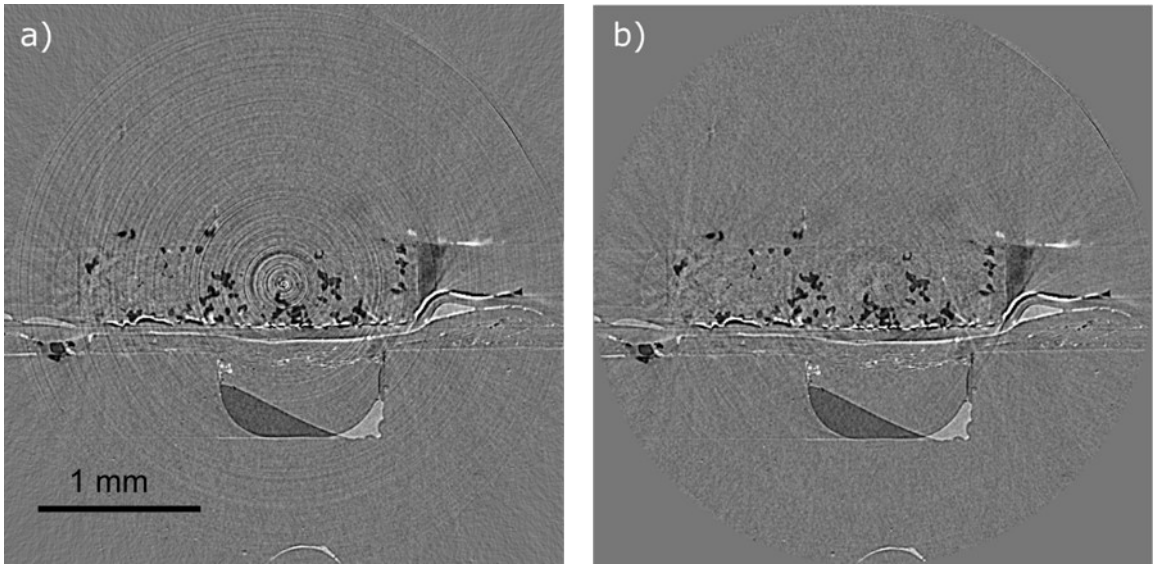

Figure S2. Comparison between the original and ring-corrected image. a) original image; b) ring corrected image.

Operando cell and design details

The endplates (EP) of the operando cell are produced by metal 3D printing, using the Aluminum AlSi10Mg alloy. The details of the cell design can be seen in Figure S3. The water inlet and the electrical contacts are placed at the bottom of the cell.

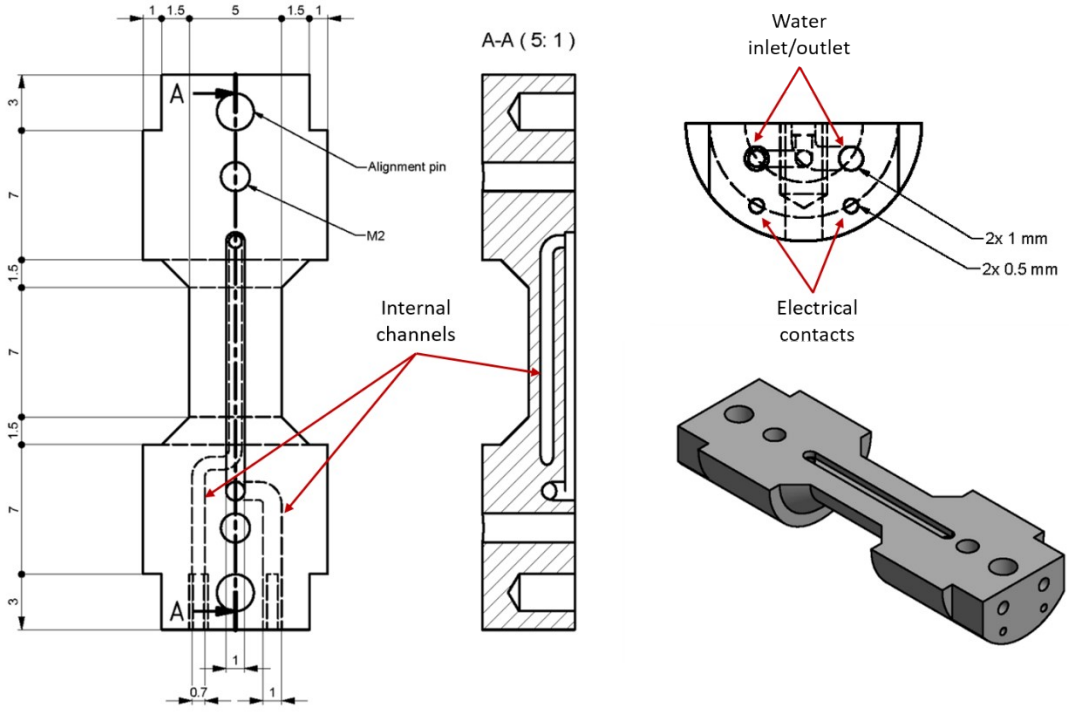

Figure S3. Details on the cell design.

The employed subgaskets and Nafion membrane are obtained by stamping out the corresponding materials using custom-designed stamping tools. Figure S3 shows the details of the stamping tools design.

Electrochemical Impedance Spectroscopy

Figure S4 shows the impedance spectra acquired at different current densities.

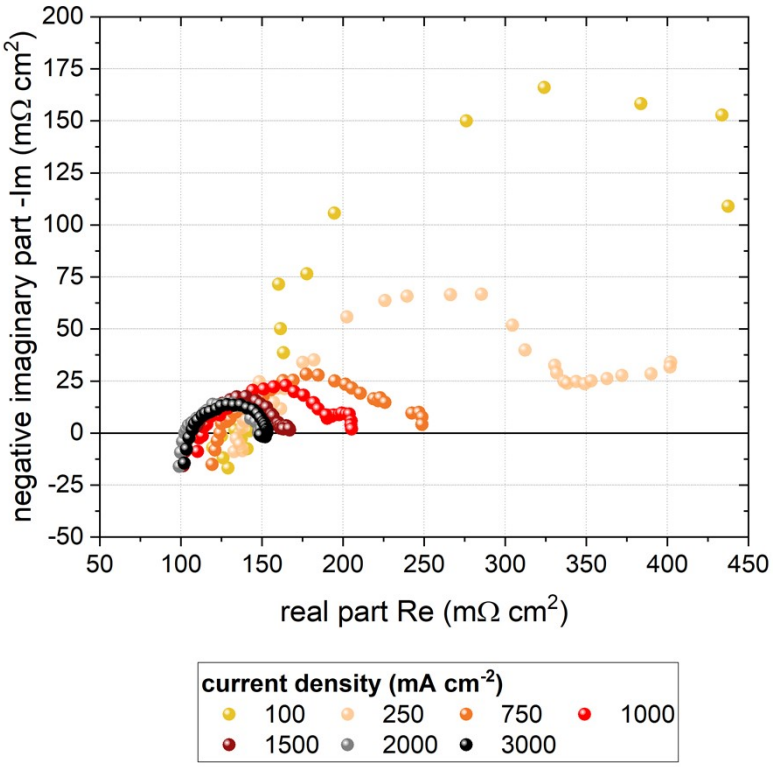

Figure S4. Impedance spectra acquired for the current densities of 100, 250, 750, 1000, 1500, 2000, and 3000 mA cm^{-2}. The spectra were acquired while the cell was operating in between the different tomographic acquisitions.

Comparison between different imaging cells employed in literature

To show the representativeness of this study, Figure S5 shows the performance of the imaging cell employed in this work compared to other *operando* cells reported in the literature: Leonard et al[5], Lee et al[6] and Satjaritanum et al[7]. For reference, Figure S5 also shows the scan time reported in these previous works.

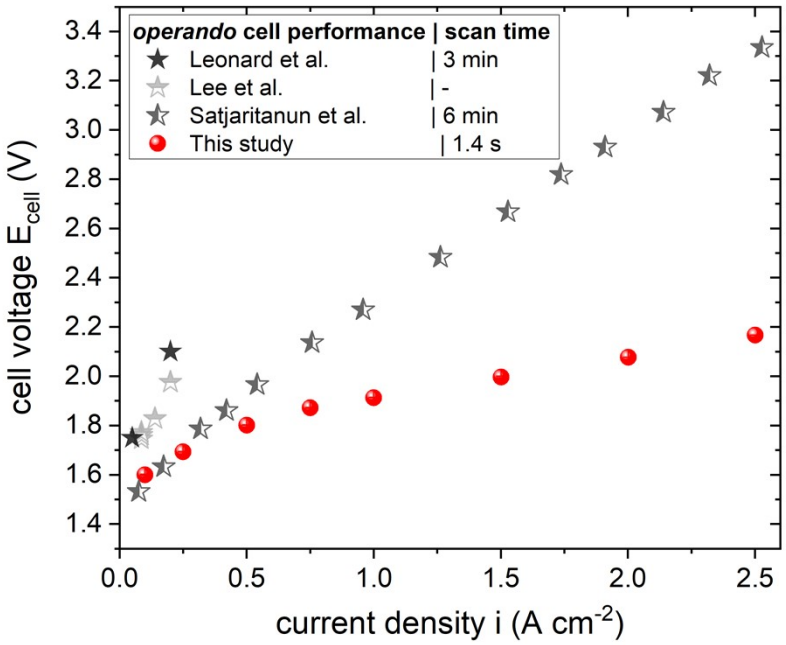

Figure S5. Performance comparison between different imaging PEWE cells employed in literature. In the legend, the scan time employed in the respective papers is also included.

References

1 N. T. Vo, R. C. Atwood and M. Drakopoulos, *Opt. Express*, 2018, **26**, 28396.
2 W. Vågberg, J. C. Larsson and H. M. Hertz, *Opt. Express, OE*, 2017, **25**, 23191–23198.
3 B. Münch, P. Trtik, F. Marone and M. Stampanoni, *Opt. Express, OE*, 2009, **17**, 8567–8591.
4 Y. Yang, Y. Yang, D. Zhang, D. Zhang, F. Yang, F. Yang, M. Teng, M. Teng, Y. Du, Y. Du, K. Huang and K. Huang, *Opt. Express, OE*, 2020, **28**, 30362–30378.
5 E. Leonard, A. D. Shum, S. Normile, D. C. Sabarirajan, D. G. Yared, X. Xiao and I. V. Zenyuk, *Electrochimica Acta*, 2018, **276**, 424–433.
6 C. Lee, J. K. Lee, B. Zhao, K. F. Fahy and A. Bazylak, *ECS Trans.*, 2019, **92**, 821–832.
7 P. Satjaritanun, M. O'Brien, D. Kulkarni, S. Shimpalee, C. Capuano, K. E. Ayers, N. Danilovic, D. Y. Parkinson and I. V. Zenyuk, *iScience*, 2020, **23**, 101783.